Macromolecules
ARTICLE

Macromolecules **2009**, *42*, 9041–9051 **9041**
DOI: 10.1021/ma901751n

Cyclic Switching of Water Storage in Thin Block Copolymer Films Containing Poly(*N*-isopropylacrylamide)

W. Wang,[†] E. Metwalli,[†] J. Perlich,[†] C. M. Papadakis,[†] R. Cubitt,[‡] and P. Müller-Buschbaum*,[†]

[†]*Physik-Department LS E13, TU München, James-Franck-Str. 1, 85747 Garching, Germany, and* [‡]*Institut Laue Langevin (ILL), 6 Jules Horowitz, 38042 Grenoble, France*

Received August 5, 2009; Revised Manuscript Received August 29, 2009

ABSTRACT: Thin films of an asymmetric diblock copolymer poly(styrene-*block*-*N*-isopropylacrylamide) (P(S-*b*-NIPAM)) with a long PS and a short PNIPAM block prepared out of a solvent which is more equal in interaction with both blocks than with water allow for water storage without significant swelling of the film. In subsequent storage and removal cycles, the aging of these P(S-*b*-NIPAM) films is investigated with atomic force microscopy, grazing incidence small-angle X-ray scattering, and in-situ neutron reflectivity. The P(S-*b*-NIPAM) films are exposed to an atmosphere of deuterated water vapor. Enrichment of the incorporated water in the film part close to the substrate interface is found. The storage capacity decreases by a factor of 2 after seven cycles, but the strongest decrease occurs in the first four cycles. This aging is discussed in the framework of an internal rearrangement of the film structure, H−D exchange, and a possible incorporation of bound water.

1. Introduction

Thin polymer films are used in various fields of application such as coatings to achieve protective, adhesive, dielectric, conducting, or resistive layers. Typically such layers are exposed to an environmental atmosphere, which contains a variety of small molecules. The most prominent example is air with its relative humidity defined by the thermodynamic parameters such as temperature and pressure. Depending on the type of small molecules, they can easily penetrate the polymer network and are incorporated inside the thin polymer film. The absorption of gases from our atmosphere such as carbon dioxide and water or exhaust fumes into polymers has nonnegligible implications for the material properties of the polymer materials. It can cause changes in thermal and mechanical properties.

Penetration of a small molecular species into an initially dry polymer film is driven by a chemical potential gradient. It is normally accompanied by swelling and plasticization of the polymer. Thus, the polymer film thickens and softens. The penetrating molecule may be a solvent or a nonsolvent of the particular polymer, depending on the thermodynamic properties of the polymer−molecule pair. A significant body of work has examined experimental and theoretical characteristics of swelling and dissolution of glassy polymer films by single organic solvent molecules.[1−10] However, with respect to application, the absorption-induced swelling of thin films can be problematic due to its related increase in film thickness, which can cause unwanted strain in a system.

Recently, it has been shown that thin diblock copolymer films can incorporate water molecules from a surrounding water vapor atmosphere, without a significant swelling of the films.[11] Thus, these films will avoid problems related to strains which are caused by swelling. The basic key for the preparation of such thin films is the installation of a glassy network which has sufficient space to incorporate water molecules but cannot increase in size. This is achieved by a thin film preparation using an asymmetric diblock copolymer poly(styrene-*block*-*N*-isopropylacrylamide) (P(S-*b*-NIPAM)) with a long PS and short PNIPAM block in combination with a solvent which is more equal in interaction with both blocks than with water. Such films allow the total water storage of 17.4% with a total film thickness increase of only 2.5%.

Poly(*N*-isopropylacrylamide) (PNIPAM) is among the most studied thermosensitive polymers.[12−32] PNIPAM in water exhibits a phase transition at a lower critical solution temperature (LCST), which has been investigated by a variety of experimental techniques in the dilute and concentrated regimes.[23−29] The LCST of PNIPAM in water is ∼32 °C and thus slightly less than body temperature, which makes PNIPAM a representative of environmental-sensitive polymers studied for biomedical applications.[33] Below the LCST the water incorporation into a PNIPAM network causes strong swelling. However, by adding hydrophobic, glassy units to the PNIPAM chain, the response and the LCST are affected. With increasing length of the hydrophobic glassy block the ability of PNIPAM to swell decreases. In most cases, polystyrene (PS) was chosen as the hydrophobic, glassy block, and diblock copolymers P(S-*b*-NIPAM),[34−37] and occasionally also triblock copolymers P(S-*b*-NIPAM-*b*-PS) were studied.[30−32,38−40] Whereas all these investigations on hydrogel systems focus on strong swelling of the thermoresponsive material, so far the nonswelling case was not focused on. Moreover, typically water is used as a solvent for the investigation of block copolymer solutions of copolymers containing PNIPAM and PS blocks and for thin film preparation (including dialysis from organic solvent into water). The direct use of organic solvents such as 1,4-dioxane is rare.[11,41]

In the present work, we probe the cyclic switching of water storage in thin block copolymer films containing PNIPAM and PS. Films with a PNIPAM volume fraction of 0.276 prepared out of 1,4-dioxane show no swelling but absorption of water. During water storage a slight reorganization of the initial microphase

*Corresponding author: Ph +49 89 289 12451, Fax +49 89 28912473, E-mail muellerb@ph.tum.de.

Published on Web 09/25/2009

separation morphology of such films was reported recently.[11] After the extraction of the stored water by applying vacuum, this changed microphase separation morphology is frozen-in, which implies that water storage causes an irreversible change of the initially installed morphology. We probe with storage cycles to what extent these morphological changes affect the water storage capability. With respect to applications of these films, such an investigation on the aging is of strong interest. The structural investigation of the cyclic water storage and removal is performed with atomic force microscopy, grazing incidence small-angle X-ray scattering, and in-situ neutron reflectivity.

In general, neutron scattering is a frequently used technique to probe the structure and structural changes in hydrogel systems and films.[42−46] With neutron reflectivity the density profile along the surface normal is accessed. In-situ measurements allow for monitoring changes in the composition during contact with a surrounding water vapor. The in-situ neutron data are accompanied by optical methods and FTIR spectroscopy.

This article has the following structure: The Introduction is followed by an Experimental Section describing the sample preparation and the experimental techniques applied. The next sections show results and discussion on the cyclic switching of the P(S-*b*-NIPAM) film.

2. Experimental Section

Materials. An asymmetric diblock copolymer of poly(styrene-*block*-*N*-isopropylacrylamide), denoted P(S-*b*-NIPAM), with a molecular weight of 23 500 g mol^{-1} and a polydispersity of 1.05 was purchased from Polymer Source Inc. The volume fraction of PNIPAM in the copolymer was 27.6%. Deuterated water (D_2O) (purity 99.95%) was from Deutero GmbH. 1,4-Dioxane was received from Acros. Dichloromethane, ammonia solutions (NH_3, 30−33%), and hydrogen peroxide (H_2O_2, 30%) were purchased from Carl Roth GmbH. Silicon (Si 100, n-type) was from Silchem.

Sample Preparation. Silicon with an oxide layer on the surface was used as substrate material for the thin P(S-*b*-NIPAM) films. For cleaning precut silicon substrates were placed in dichloromethane in an ultrasonic bath at 46 °C for 30 min and rinsed with Millipore water shortly after. Afterward, the substrates were kept for 2 h in an oxidation bath at 75 °C consisting of 1400 mL of Millipore water, 120 mL of H_2O_2, and 120 mL of NH_3 to clean the surface from organic traces and install a hydrophilic surface. Thereafter, the substrates were stored shortly in Millipore water. Directly before spin-coating the substrates were rinsed with Millipore water for at least 10 min to remove possible traces of the oxidation bath. The substrates were dried with compressed nitrogen before coating. Because of this protocol, at the Si surface an oxide layer of 1 nm is present, which has a surface roughness below 0.5 nm.[47]

The initial dry P(S-*b*-NIPAM) films with different thicknesses were prepared with spin-coating (2000 rpm, 30 s) from a 1,4-dioxane solution at room temperature onto these precleaned Si substrates.

Storage Cycle Protocol. The initial dry P(S-*b*-NIPAM) film of the desired film thickness was mounted in a custom-made vapor chamber in air, thermostated to 23 °C, and investigated. To start the first storage cycle, the vapor chamber was evacuated, and the water reservoir of the vapor chamber was filled with D_2O to install a saturated D_2O atmosphere. The addition of D_2O marks the starting point of the water absorption kinetics (time = 0). After reaching equilibrium of water storage (240 min) the film is fully swollen. The removal of D_2O was initiated by pumping the vapor chamber through a vacuum pump (DIVAC 0.8 T, Leybold AG). Thus, water release from the thin film occurs, and the P(S-*b*-NIPAM) film relaxes back in vacuum to a new dry state. This deswollen film was used in the next storage cycle as the initial dry film (see Scheme 1). To address aging effects of the water storage, the storage and removal cycles were repeated seven times. Samples were investigated in-situ during these cycles with neutron reflectivity and ex-situ after individual cycles with the other experimental techniques.

Scheme 1. Applied Storage and Removal Cycle

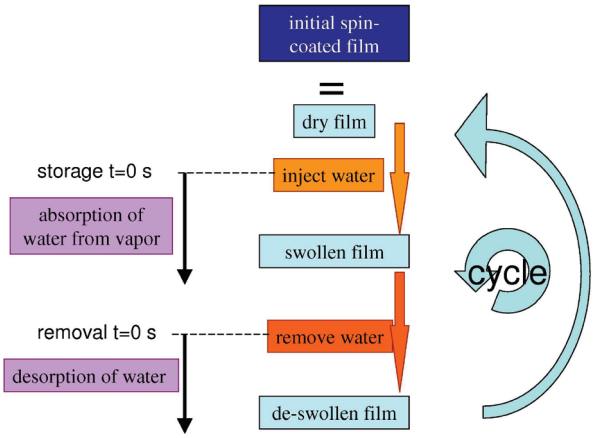

For the investigated range of P(S-*b*-NIPAM) film thicknesses no delamination was observed. However, very thick films exhibit delamination from the substrate in such cycles.

Neutron Reflectivity and Off-Specular Scattering. The neutron scattering experiments were carried out at the D17 instrument at ILL, Grenoble, in time-of-flight (TOF) mode.[48] TOF mode allowed for the collection of specular and off-specular scattering data, in which neutrons with a broad range of wavelength λ were used simultaneously and registered as a function of their respective times of flight. The necessary pulsing of the beam was realized by a double chopper system. The largest available sample−detector distance of 3.4 m was operated. The diffracted intensity was recorded on a two-dimensional (2d) detector without the movement of any motors. The absence of motor movements was crucial for achieving a high time resolution as well as for avoiding mechanically induced vibrations which might destabilize swollen films (by activation of long wavelength surface waves). On the detector the counts were registered for each spatial pixel (x, y) as a function of TOF in 1000 channels. After integration of the counts for fixed x and TOF channel along the vertical detector axis y, and the TOF to λ conversion, the scattered intensity is displayed as a function of λ and the exit angle α_f. Finally, the corrected data set $I(\alpha_f,\lambda)$ can also be transformed to $I(q_x,q_z)$ with the given (constant) angle of incidence $\alpha_i = 0.5°$, where q_z denotes the wave vector component perpendicular to the surface and q_x the one in the surface in parallel to the neutron beam.

Kinetic changes due to the applied storage and removal cycles were probed by performing reflectivity scans every 30 s. The initial dry P(S-*b*-NIPAM) film used for cyclic switching, and the resulting deswollen P(S-*b*-NIPAM) film at the end of each cycle was additionally probed with an increased counting time of 3600 s. The probed q_z range between 0.01 and 0.85 nm^{-1} is selected to cover the critical edges of protonated (Si and P(S-*b*-NIPAM)) and deuterated (D_2O) substances. All reflectivity curves were fitted with the Motofit program[49] with appropriate error weighting and point-by-point resolution smearing. An automated batch fit approach is taken, with all the data sets being analyzed in series. The scattering length densities of 2.07×10^{-6} Å^{-2} for Si, 3.47×10^{-6} Å^{-2} for Si oxide, 1.30×10^{-6} Å^{-2} for P(S-*b*-NIPAM), and 6.36×10^{-6} Å^{-2} for D_2O were fixed from initial fits and agree with literature values.

X-ray Reflectivity. X-ray reflectivity measurements were carried out with a laboratory X-ray source instrument (D5000 from Siemens) with a Cu target (wavelength $\lambda = 0.154$ nm). The beam was collimated by a slit system. A knife edge collimator (KEC)

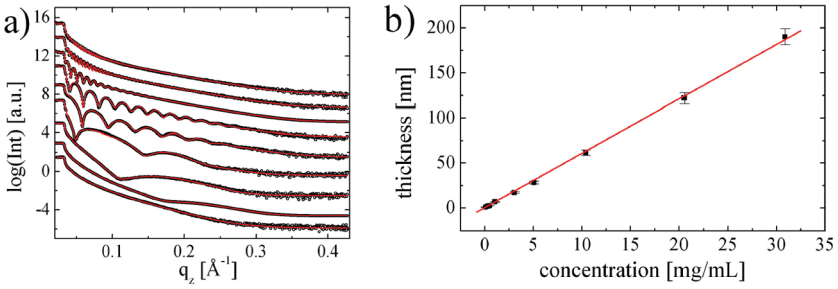

Figure 1. (a) X-ray reflectivity data (dots) shown together with model fits (lines) for the thickness regime covered in this investigation. With increasing thickness (0.8, 1.7, 2.5, 6.6, 17.1, 28.1, 61.4, 121.8, and 190 nm from bottom to top) the curves are shifted along the *y*-axis for presentation. (b) Film thickness plotted as a function of the P(S-*b*-NIPAM) concentration of the 1,4-dioxane solution used for spin-coating. The solid line is a linear fit.

was placed directly above the sample center to define the illuminated surface area and avoid overillumination at small incident angles. The reflected intensity was detected with a scintillation counter, which was prevented from saturation by using an automatic beam absorber system. A typical $\theta-2\theta$ scan was performed in a range of 2θ from 0° to 4.5°. To obtain the density profile perpendicular to the substrate surface, the reflectivity data were fitted with the Parrat algorithm.[50]

Grazing Incidence Small-Angle X-ray Scattering. The grazing incidence small-angle X-ray scattering (GISAXS) measurements were performed at the synchrotron beamline BW4 at the DORIS III storage ring at the DESY HASYLAB facility in Hamburg, Germany. Synchrotron radiation with a wavelength of $\lambda = 0.138$ nm was used; the beam shape in and out of the plane of reflection was set by two entrance cross slits. For the experiment, an assembly of beryllium compound refractive lenses provides a moderately microfocused beam size of smaller than $30 \times 20\ \mu m^2$ (vertical × horizontal), which also enables the investigation of local gradients of the thin film morphology.[51] The highly intense direct or transmitted beam is blocked by a diode beam stop in front of the detector. In order to block the specularly reflected beam on the detector, a pointlike movable specular beam stop was installed. For the measurement, the sample was placed horizontally on a goniometer. The angle of incidence was set to $\alpha_i = 0.421°$, which is above the critical angles α_c of the investigated block of the diblock copolymers (PS: 0.138°; PNIPAM: 0.148°). Hence, the Yoneda peak is separated from the specular peak on the detector, and both the sample surface and the interior of the film are probed. A 2D detector (MarCCD 165 by Mar Research, 2048 × 2048 pixels) to record the scattering intensities is positioned with a sample-to-detector distance of $D = 2.115$ m behind the sample. From the recorded 2D intensity distribution, structural information on the sample can be extracted from horizontal and vertical cuts (with respect to the sample surface).[52] The vertical cut, called the detector cut, at a horizontal angle of $\Psi = 0°$, corresponding to $q_y = 0$, contains information about structures perpendicular to the surface (e.g., the correlated roughness) as well as the material-specific Yoneda peak at $\alpha_f = \alpha_c$. Horizontal cuts, called out-of-plane cuts (q_y cuts) or GISAXS cuts, are performed at constant q_z and are selected according to the q_z condition ($\alpha_f = \alpha_c$). From the q_y cuts, lateral structure information (e.g., geometry, size distribution, and spatial correlation) is extracted. In order to improve statistics, the intensity of q_y cuts in a narrow range of Δq_z is integrated.

Optical Interference Measurements. Thickness and optical constants (n and k) were measured with the Filmetrics F20 Thin-Film Measurement System (Filmetrics Inc., San Diego). The spot size of the light beam is adjustable from 500 μm to 1 cm. The characteristic intensity oscillations in the reflectance spectrum are analyzed in a wavelength regime from 340 to 1100 nm.

FTIR Spectroscopy. The H−D exchange reaction between P(S-*b*-NIPAM) and D_2O was measured with FTIR spectroscopy using a JASCO FTIR-4100 spectrometer. The PS-*b*-PNIPAM dry film was prepared by solution-casting from a 1,4-dioxane solution on a MIRacle diamond substrate. The film thickness was in the range of 1−3 μm. Next, the P(S-*b*-NIPAM) film was exposed to a saturated D_2O atmosphere at 23 °C for 30 min. Afterward, the P(S-*b*-NIPAM) film was dried in air at 23 °C for 15 min before the FTIR measurement. For comparison, a second dry P(S-*b*-NIPAM) film was prepared and treated in the same way but with H_2O replacing the D_2O used before. The experiments were repeated to ensure reproducibility of the reported results.

Optical Microcopy. The sample surfaces were observed with optical microscopy using a Zeiss Axiotech 25H optical microscope with magnifications between 5× and 100×. A Hitachi KP-D50 CCD camera recorded the micrographs.

Atomic Force Microcopy. The surface topography was imaged with atomic force microscopy (AFM) in tapping mode condition. A phase shift micrograph was recorded to distinguish between hard and soft materials. The measurements were carried out with an Autoprobe CP Research AFM instrument on dry films in ambient air atmosphere at room temperature. Gold-coated silicon cantilevers (Ultralever cantilevers) with a resonance frequency of 75 kHz and a spring constant of 2.1 N/m were used. The used tip had an asymptotic conical shape with a high aspect ratio and a curvature radius of 10 nm which is small as compared to the measured structures. To improve the accuracy of the AFM height and lateral information, calibration was performed with calibration standards.

3. Results and Discussion

a. Initially Spin-Coated Films. Using 1,4-dioxane solutions P(S-*b*-NIPAM) films of different thicknesses were prepared on Si with spin-coating. To obtain a large range of different film thickness, the concentration of the solutions used for spin-coating was varied from 0.1 to 30 mg/mL. The spin-coating parameters (spinning speed, acceleration, and spinning time) were kept fixed and films were prepared at room temperature. With optical microscopy the surfaces appear smooth and continuous. No large-scale heterogeneities are observed. Thus, the P(S-*b*-NIPAM) films behave with respect to surface structures very similar to films of end-capped PNIPAM prepared from dioxane solutions,[41] whereas it was reported that very thick (bulklike) PNIPAM gel films (thicknesses on the order of 60 μm) were inhomogeneous on a micrometer scale.[53]

The X-ray reflectivity measurements at the initial spin-coated films confirm the film homogeneity observed with optical microscopy, except for an extremely thin film (thickness of 0.8 nm). Figure 1a shows the corresponding data for a selection of dry P(S-*b*-NIPAM) films. From the bottom to the top, the film thickness increases from 0.8 to 190 nm. All reflectivity curves, with the exception of the data from the thinnest film, exhibit well-pronounced fringes, which extend to large values of the scattering vector component q_z. So for film thicknesses larger than 0.8 nm we obtain

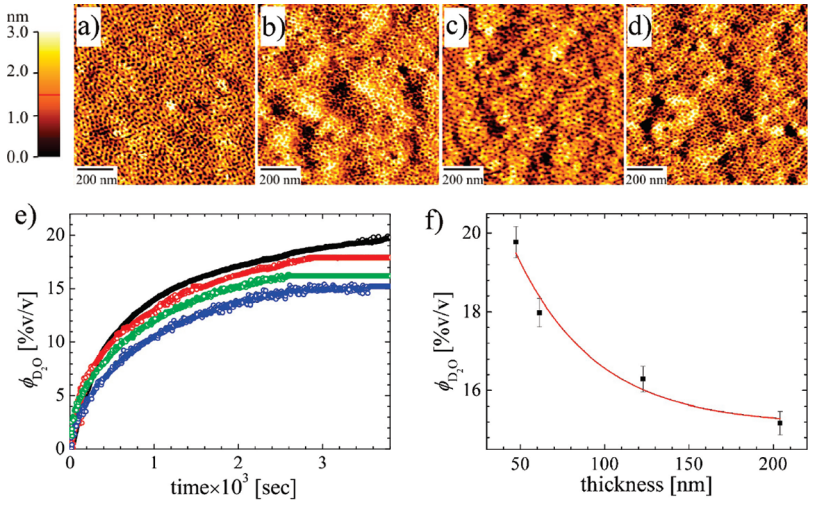

Figure 2. Topography AFM images of P(S-*b*-NIPAM) films with different thicknesses: (a) 17.1, (b) 28.1, (c) 121.8, and (d) 204 nm. The scan area is 1 μm × 1 μm for all AFM images. The structure height increases with the brightness of the structures in the images. The height scale bar range is 0−3 nm. (e) Time-dependent changes of the water uptake for different thicknesses. From top to bottom the thickness decreases: 47 (black), 61.4 (red), 121.8 (green), and 204 nm (blue). (f) Water uptake as a function of film thickness.

homogeneous films with a small surface roughness. For smaller film thicknesses, represented by the thinnest film (0.8 nm), the fringes in the reflectivity curve are strongly damped due to the imperfections of the block copolymer layer.

Although spin-coating is a widely used process, its theoretical description is complicated and even in the case of simple homopolymers not fully understood. Therefore, typically in literature empirical relations are used to describe the dependence of the obtained film thickness of the spinning parameters or the concentration.[54−56] Figure 1b shows that the linear dependence of the resulting dry film thickness on the concentration used for spin-coating is valid for the investigated diblock copolymer P(S-*b*-NIPAM), if spin-coated from 1, 4-dioxane solutions. From Figure 1b it is easily possible to prepare P(S-*b*-NIPAM) films of the desired thickness in a reproducible way. This saves material and allows for experiments with the film thickness as control parameter.

To probe the surface structure of the P(S-*b*-NIPAM) films with high resolution, atomic force microscopy (AFM) is used. Figure 2a−d shows an example of topography data having a scan size of 1 μm × 1 μm to emphasize local surface structures for dry film thickness of 17.1, 28.1, 121.8, and 204 nm. In this range of film thicknesses, all films have a surface structure on the nanometer scale, which is caused by the microphase-separation morphology of P(S-*b*-NIPAM). In contrast for very thin films, such as for 0.8 nm film thickness, only large polymer islands (180−250 nm in diameter) are observed. The Si substrates are no more homogeneously covered, if the material present is insufficient to form a complete P(S-*b*-NIPAM) film. This incomplete surface coverage causes a large surface roughness (peak-to-valley amplitude equal to the film thickness), which explains the absence of fringes in the X-ray reflectivity data. During the spin-coating dewetting occurs which was observed in case of many other polymer−solvent pairs as well.[57] However, in case of hydrogel films dewetting so far has not been investigated in detail.[45] In contrast, alternative routes for patterning were applied, such as techniques based on lithography[58−60] or on the self-organization in thin soft films when they are confined by adhesive forces such as the van der Waals and electrostatic forces.[61]

At higher concentration, continuous films are formed, which exhibit a surface structure reflecting the microphase-separated structure of the diblock copolymer. With increasing film thickness, the surface structures coarsen laterally and become more oriented, whereas the height of the surface structures (peak-to-valley amplitude) decreases from 2 to 0.5 nm. Hence, a simple way to control the film thickness for water storage applications of the glassy thin P(S-*b*-NIPAM) films is at hand by varying the concentration of the P(S-*b*-NIPAM) solutions. With respect to applications requiring homogeneous films, the film thickness range from 1.7 to 204 nm is accessible.

b. Comparison between Dry and Cycled Films. With optical interference measurements the time-dependent swelling of the P(S-*b*-NIPAM) films was examined as a function of film thickness. All homogeneous films show no increase in film thickness during water uptake. The incorporation of water causes only a change in the refractive index, which is used to determine the amount of water stored inside the film. The kinetics of water uptake are shown for four selected film thickness in Figure 2e. Interestingly, with increasing film thickness the ability to include water into the film decreases (see Figure 2f).

Out of the accessible film thickness range for the storage and removal cycles one fixed film thickness was selected to accommodate with the limited available neutron beamtime. We selected a P(S-*b*-NIPAM) film thickness of 47 nm, which is on the one hand not in the extremes of the accessible film thickness range and on the other hand marks a good candidate for application. With neutron reflectivity, GISAXS, and AFM the initial dry P(S-*b*-NIPAM) film and the same film after each cycle are probed (see Scheme 1). Figure 3 shows the corresponding AFM data, giving information about changes in the film surface.

The perpendicularly oriented cylindrical domains of PNIPAM in the PS matrix are quite distinct in all the images. The domain size is ∼20 nm in diameter. Upon increasing water storage cycles, the surface roughness of the P(S-*b*-NIPAM) film increases slightly, the cylindrical domains become more and more distorted, and some larger structures arise up on the film surface. Regarding the film surface the aging of the P(S-*b*-NIPAM) film starts significantly with the fourth cycle. However, the local microphase separation structure remains unchanged in size.

To get information about changes of the structure inside the P(S-*b*-NIPAM) film, neutron reflectivity is used. Figure 4 shows the corresponding data and the resulting scattering length density (SLD) profiles.

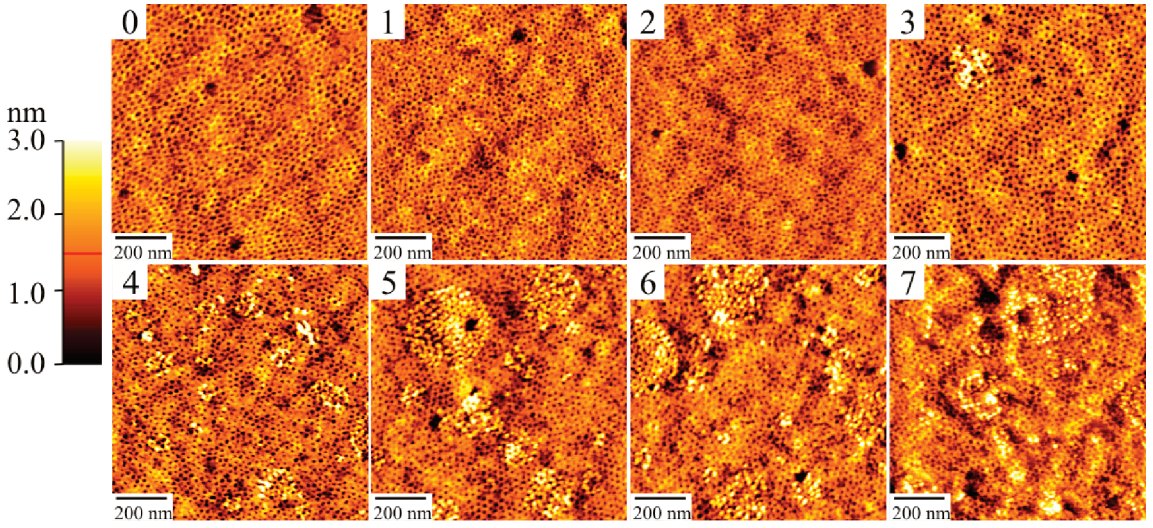

Figure 3. Topography AFM images of P(S-*b*-NIPAM) films before water storage (0) and after seven water storage cycles (1−7). The scan area is 1 μm × 1 μm for all AFM images. The structure height increases with the brightness of the structures in the images. The height scale bar range is 0−3 nm.

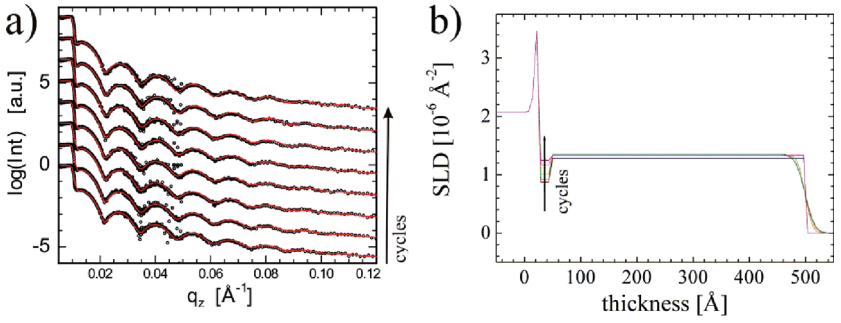

Figure 4. (a) Neutron reflectivity data (dots) shown together with model fits (lines) for the 47 nm thick P(S-*b*-NIPAM) film initially prepared (bottom curve) and measured after complete storage and removal cycles (number of cycles increases from bottom to top). (b) Resulting scattering length density (SLD) profiles show a bilayer structure on top of the Si substrate.

Whereas for X-rays the P(S-*b*-NIPAM) film appears mostly homogeneous along the surface normal due to the negligible contrast, due to the much larger contrast in neutron reflectivity an internal structure is resolved. The initially spin-coated, dry film has to be described as a bilayer. The bottom layer, namely the part of the polymer film which is directly in contact with the substrate (denoted interface part), has an SLD of 0.87 × 10^{-6} Å^{-2} and a thickness of 1.9 nm. Because the SLD of the pure PNIPAM bulk material from the literature is 0.869 × 10^{-6} Å^{-2},[62] we conclude that close to the Si substrate a purely PNIPAM containing layer is present. In contrast, the top layer, namely the part of the polymer film which is in contact with air (denoted main part), has an SLD of 1.31 × 10^{-6} Å^{-2}. This top layer has a thickness of 45.5 nm and an average roughness of 0.5 nm. Therefore, the main part of the film consists of P(S-*b*-NIPAM). The interface enrichment of PNIPAM can be explained by the hydrophilicity introduced by the chemical treatment of substrate used for cleaning of the Si.[11] The substrate has a hydrophilic oxide layer with a water contact angle of 0° (water can spread on the surface).[63] This hydrophilic oxide layer has a very strong attraction to the PNIPAM segments, and a high volume fraction of PNIPAM segments is located at the interface with the substrate.

After each storage and removal cycle, the neutron reflectivity data are only slightly changed. Thus, each storage and removal of water does not have a dramatic influence on the P(S-*b*-NIPAM) film. However, a careful inspection of the resulting SLD profiles (see Figure 4b) shows slight changes. Fitting with a bilayer model is still necessary, but the SLD of both layers changes with cycle number and the surface roughness increases in good agreement with the AFM data. In contrast, the thicknesses are not affected, which gives a first hint that the investigated P(S-*b*-NIPAM) film is well suited for cyclic storage applications and aging does not destroy the film.

With increasing cycle number the SLD values increase, which can only be explained by the irreversible incorporation of D_2O used in the investigation of the cyclic switching or by an H−D exchange reaction happening during the water storage.

In principle, simultaneously with the neutron reflectivity at D17 the off-specular neutron scattering was measured as well. This off-specular scattering showed an increase in intensity with increasing number of swelling cycles due to a buildup of an internal disorder. However, detailed modeling of such off-specular neutron data is rather complicated, and only information about large-scale structures is obtained. Because grazing incidence small-angle neutron scattering (GISANS) is strongly flux limited, we used GISAXS to obtain information about lateral structures inside the P(S-*b*-NIPAM) film on the scale of the microphase separation structure. In GISAXS the contrast is less favorable as compared with GISANS, but as visible in Figure 5 the inner film structure is well resolved.

Figure 5 shows the vertical and horizontal cuts from the 2D GISAXS intensity. From the vertical cuts, we can find that the perpendicular structure (correlated roughness,

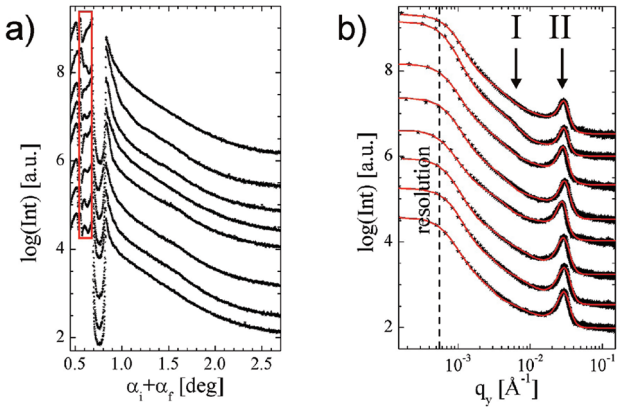

Figure 5. GISAXS data of P(S-*b*-NIPAM) films before water storage (bottom curve) and after seven water storage cycles (subsequently shifted seven curves): (a) vertical cuts showing structures along the surface normal and (b) horizontal cuts (dots) displayed together with model fits (lines) showing in-plane structures.

highlighted by the box in Figure 5a) is damped with increasing cycle number. So the initially long-ranged correlated P(S-*b*-NIPAM) film becomes independent in its surface structures from the substrate by slight roughening.

In the horizontal cuts, one well pronounced peak (denoted with II in Figure 5b) is present from the beginning and a second broad and shoulder-like peak (denoted with I in Figure 5b) is building up in the last cycles. The intense peak is caused by the microphase separation structure, and from a fit to the data we obtain a structural length of 21 nm. This value is in good agreement with the AFM data and represents the distance between adjacent PNIPAM cylinders in the PS matrix. During cycling the microphase separation structure is not changed (neither swollen nor shrunk), which is a good argument to exclude residual solvent being present inside the P(S-*b*-NIPAM) film after a finished storage and removal cycle. Only the peak intensity is slightly decreasing with increasing cycle number shown a slight disordering of the PNIPAM cylinders inside the PS matrix.

During the cycling of the film a second and larger structure growing causing the shoulder-like peak. This larger structure is domains on the size of 150 nm which are seen to some extent with AFM on the film surface as well. Thus, the perturbance of the structure yields domains inside the film and at the film surface which cause the main aging of the P(S-*b*-NIPAM) film.

c. Water Storage and Removal Cycles. For a deeper understanding of the aging the water storage and removal is probed with in-situ neutron reflectivity and off-specular scattering. In-situ GISAXS measurements are impossible due to radiation damage occurring at swollen P(S-*b*-NIPAM) films. Anyhow, the contrast necessary for determining the water content in the thin P(S-*b*-NIPAM) film is gained from the use of deuterated water (D_2O) in combination with the protonated polymer in a neutron scattering experiment. In a kinetic experiment the initially prepared dry glassy film is exposed cyclicly to water vapor (see Scheme 1), and with in-situ neutron scattering measurements the changes of the film due to storage of water are monitored. In Figure 6a, a representative 2D detector pattern of the scattered intensity (displayed as a function of wavelength λ and the exit angle α_f) is shown.

Because off-specular intensities are significantly lower than the specular ones, a detailed analysis of intensity as a function of lateral wavevector component q_x is impossible for the kinetic data. The necessary improvement of statistics

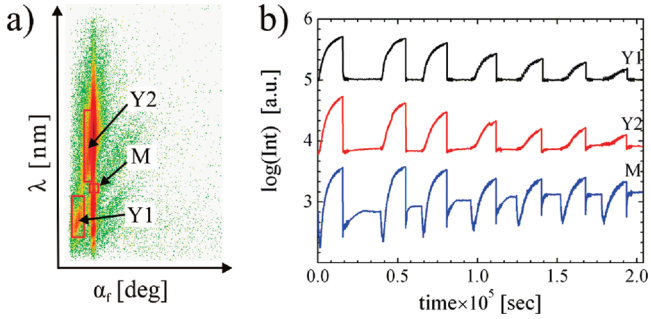

Figure 6. (a) Representative 2d detector pattern of scattered intensity displayed in the wavelength λ vs exit angle α_f presentation. The red boxes mark the area integrated for the analysis of diffuse scattering. (b) Intensities integrated over the areas Y1, Y2, and M (as explained in the text) shown on a logarithmic axis as a function of time for the seven storage and removal cycles. The curves are shifted along the *y*-axis for presentation.

is achieved by an integration of off-specular intensities. Thus, to maintain the very high time resolution (30 s) of the scattering experiment and to account for the kinetic changes of the films due to water storage and removal, integration is performed in *q*-space rather than in the time domain. The red boxes in Figure 6a mark selected regions in the intensity, which are used for integration and further analysis: integration region of the specularly reflected intensity (M) and off-specular scattered intensities—Yoneda peak intensities of deuterated material (Y1) and protonated material (Y2).

Figure 6b shows the time evolution of specular reflectivity (M) and off-specular reflectivities (Y1, Y2) for the seven repetitive cycles of water storage and removal. Because of the incorporation of D_2O, the scattering length density (SLD) of the film increases, resulting in the increase of the reflected intensity and shift of the position of the total reflection edge toward a smaller λ value. Accordingly, the intensity in the region M increases with absorption of D_2O. The off-specular intensities Y1 and Y2 increase with time due to the buildup of a lateral structure inside the glassy block copolymer film because D_2O selectively diffuses into parts of the film. After the vapor is extracted, both of the specular and the off-specular intensities decrease to the initial state of the water storage immediately and reach stability after 2.5 h. However, with increasing cycle number the actual intensity values change, and only the overall shape stays unchanged. As expected in terms of an aging process, the amplitudes decrease from cycle to cycle.

A more detailed analysis of the time evolution of water storage in the glassy hydrogel film is achieved by fitting the individual neutron reflectivity curves. From these fits the total P(S-*b*-NIPAM) film thickness and water penetration (% v/v) are determined.

The injection of D_2O marks the start of the water-absorbing process for each cycle (see Scheme 1). In the first cycle, from the beginning of the D_2O penetration until the saturation is reached, the total thickness of the film only increased by 1.2 nm, with the thickness of the interface part of the film (bottom layer) increasing by 0.25 nm. So in total, the glassy hydrogel film increases its thickness only by 2.5%, which is the key point for applications. In detail, the interface part (bottom layer) swells by 10.8% in height which is much more than the main part (top layer), which swells only 2.2% in height. It indicates that the high PS volume fraction seriously reduces the swelling capability of the P(S-*b*-NIPAM) film as the bottom layer mainly consists of PNIPAM. As the solid substrate is not deformable and thus the swelling can only

happen in the direction normal to the surface, we can conclude that the volume of the whole P(S-*b*-NIPAM) film only increased by 2.5%.[11]

From the changes of the SLD values, the D_2O volume fraction Φ_{D_2O} of the film is calculated using

$$\phi_{D_2O} = \frac{n - n_1}{n_2 - n_1} \quad (1)$$

where n denotes the in-situ probed SLD of the film, n_1 the initial SLD of the dry film, and n_2 the SLD of D_2O. In Figure 7a,b, the time evolutions of the D_2O volume fraction Φ_{D_2O} of the top layer and the bottom layer are presented. As known from the initial water absorption,[11] both parts of the P(S-*b*-NIPAM) film behave differently and two different kinetic behaviors are observable.

The water absorption of the main part of the film, given by the top layer, can be divided in two different regimes. We denote them by stage I and II (see Scheme 2). In the first regime (stage I, $0-1.22 \times 10^3$ s), the water storage rate first increases rapidly and then reaches a plateau. D_2O vapor molecules enter into the porous structure of the block copolymer film and diffuse into all accessible volume of the film. During this mass uptake the initial film structure stays unchanged as proven by the off-specular scattering shown in Figure 6b because the integrated values of the off-specular intensities Y1 and Y2 show nearly no increase, meaning that D_2O has not yet selectively diffused into the PNIPAM domains in this stage. As a consequence, the D_2O volume fraction Φ_{D_2O} of the top layer is increased to 5% irrespective of the cycle number. Obviously, the accessible porous structure is not affected by the cyclic switching of the P(S-*b*-NIPAM) film. In the second regime (stage II, 1.22×10^3 s−end) the coiled PNIPAM chains start to swell and attract selectively D_2O molecules because PNIPAM is soluble in D_2O, which causes a strong attractive interaction between them, whereas the net interaction between the polymer segments of the copolymer is repulsive. This causes a strong increase of the integrated off-specular intensities Y1 and Y2 (see Figure 6b). An internal contrast is built up due to enrichment of D_2O in selected domains and a reorganization of the initial microphase separation morphology. Because PS has a strong repulsive interaction with D_2O and PNIPAM, the PNIPAM chains initially can only swell to the free volume space between the PS and PNIPAM domains, which is formed due to the phase separation between PS and PNIPAM, until maximum water storage is reached. With increasing cycle number this maximum value decreases.

The water absorption of the very thin interface part of the P(S-*b*-NIPAM) film, which consists of pure PNIPAM, behaves differently from the majority of the film (see Figure 7b). Only a single regime is discovered in the increase in the absorbed water from the increase in SLD. Similar to the second regime probed for the main part of the film, the ability to incorporate water decreases with increasing cycle number. However, the effect is not as strong as for the main part of the film.

The swelling kinetics of a spherical gel was formulated by Tanaka and Fillmore on the basis of a cooperative diffusion theory,[64] wherein the shear modulus was considered to be negligible in comparison with the osmotic compressive modulus. By including a non-negligible shear modulus, Peters and Candau[65] developed a general model to characterize the swelling kinetics of spherical, cylindrical, and disklike polymer gels. Later, Li and Tanaka[66] proposed a two-process mechanism after realizing that neither gel swelling nor shrinking can be considered to be a pure diffusion process.

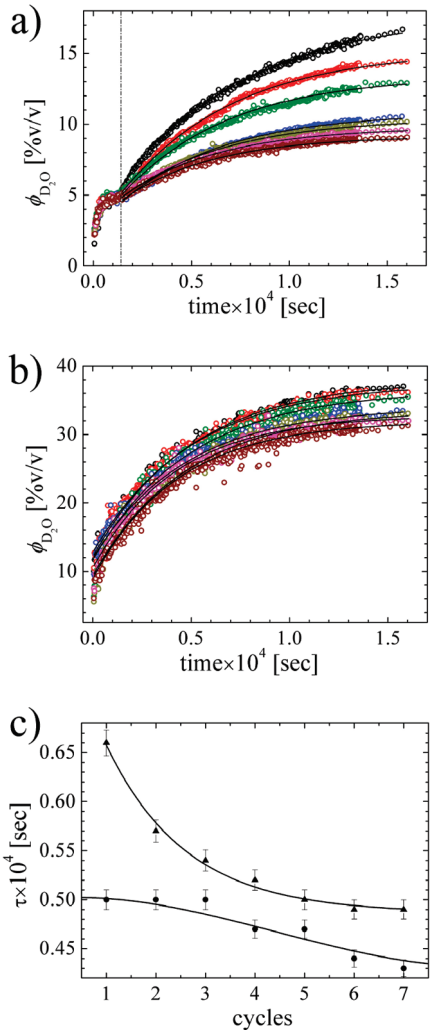

Figure 7. Water absorption inside the P(S-*b*-NIPAM) film as a function of time for the seven storage cycles: (a) for the main part of the film (top layer) and (b) for the interface part of the film (bottom layer). From top to bottom: black, red, green, blue, dark yellow, magenta, and dark red wine circles represent cycle number 1 to 7, respectively. Lines in panels (a) and (b) are fits of Eq. 4. (c) Time constants τ determined for the storage kinetics of each individual cycle for the main (circle) and interface (triangle) part of the film.

Scheme 2. Structural Evolution during the Applied Storage and Removal Cycles[a]

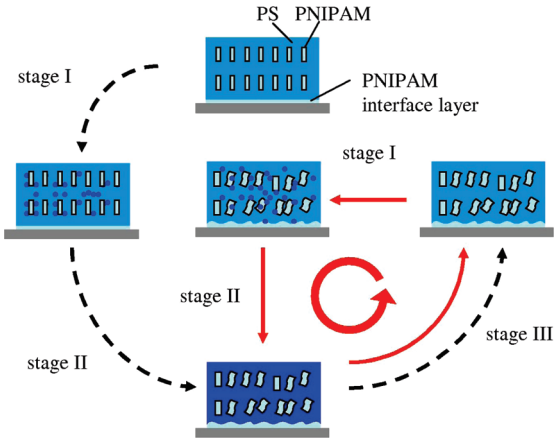

[a] The initial cycle is indicated by the dashed arrows and the all subsequent cycles with the solid arrows. Dark blue dots represent water. The changes are exaggerated.

They predicted that the shear modulus (M_{shear}) is related to the net osmotic modulus (M_{os}) and the osmotic bulk modulus (K_{bulk}) by[66]

$$R = \frac{M_{shear}}{M_{os}} = \frac{M_{shear}}{K_{bulk} + \frac{4}{3}M_{shear}} \quad (2)$$

According to Li and Tanaka, the swelling or shrinking follows

$$\frac{\phi_{D_2O}(\infty) - \phi_{D_2O}}{\phi_{D_2O}(\infty)} = \sum_{n=1}^{\infty} B_n \exp\left(-\frac{t}{\tau_n}\right) \quad (3)$$

where ϕ_{D_2O} and $\phi_{D_2O}(\infty)$ are the solvent uptake at time t and infinite time (i.e., at equilibrium), respectively; $[(\phi_{D_2O}(\infty) - \phi_{D_2O})/\phi_{D_2O}(\infty)]$, the relative swelling capacity at time t; B_n, a complicated function of R; and τ_n, the relaxation time related to the nth mode. When $t \gg 1$ or $\tau_1 \gg \tau_n$ ($n \geq 2$) or $B_1 \gg B_n$ ($n \geq 2$), all high-order terms ($n \geq 2$) in eq 3 can be dropped. In this case, the swelling and shrinking follows a first-order kinetics, i.e.

$$\ln\left(\frac{\phi_{D_2O}(\infty) - \phi_{D_2O}}{\phi_{D_2O}(\infty)}\right) = \ln B_1 - \frac{t}{\tau} \quad (4)$$

where B_1 is related to R by[66]

$$B_1 = \frac{2(3-4R)}{\alpha_1{}^2 - (4R-1)(3-4R)} \quad (5)$$

and τ_1 is related to the collective diffusion coefficient D_c by

$$D_c = \frac{3Z_\infty{}^2}{\tau_1 \alpha_1{}^2} \quad (6)$$

with α_1 being a function of R, i.e.

$$R = \frac{1}{4}\left[1 + \frac{\alpha_1 J_0(\alpha_1)}{J_1(\alpha_1)}\right] \quad (7)$$

and Z_∞ being the disk thickness in the final swelling equilibrium state, where J_0 and J_1 are the zeroth- and first-order Bessel functions. In case of a thin film Z_∞ is replaced by the part of the thickness of the film which is occupied by water. The t-dependence of $[(\phi_{D_2O}(\infty) - \phi_{D_2O})/\phi_{D_2O}(\infty)]$ can lead first to B_1 and τ_1 and then to R and D_c on the basis of eqs 4−7.

Figure 7a shows the water uptake of the main part of the film versus time. At $t \rightarrow \infty$ the maximum water uptake $\phi_{D_2O}(\infty)$ is reached. On the basis of eq 4, B_1 and τ_1 were determined by fitting. As visible in Figure 7a, we can describe the main part of the swelling of the thin P(S-*b*-NIPAM) film by the first-order kinetics (eq 4). Table 1 summarizes the values of $\phi_{D_2O}(\infty)$, τ_1, B_1, R, and D_c of the main part of the film.

In case of a thin gelatin gel film the value of R is about 0.67,[67,68] and for macroscopic sized gels[66,69] the value of R is in a range from 0.3 to 0.4, which are comparable to the values we get. According to the definition of R, the decrease of R during cycling means K_{bulk} increases faster than M_{shear}. The value of B_1 is 0.71 for very thick disklike gels (1.33 mm in thickness)[66] and 0.87−0.95 for thick films (60 μm in thickness).[67] τ_1 is 1.3×10^4 s for the disklike gels[66] and $(0.05-0.16) \times 10^4$ s for thin films.[67] Again, our determined values cover this range and are decreasing with cycle number.

Table 1. Values of $\phi_{D_2O}(\infty)$, τ_1, B_1, R, and D_c of the Main Part of the P(S-*b*-NIPAM) Film

cycle no.	$\phi_{D_2O}(\infty)$	$\tau_1/10^4$ s	B_1	R	$D_c/10^{-15}$ cm^2/s
1	17.8	0.66	0.85	0.55	4.59
2	15.2	0.57	0.85	0.55	5.09
3	13.2	0.54	0.82	0.53	4.71
4	10.8	0.52	0.77	0.44	3.52
5	10.4	0.52	0.71	0.34	2.79
6	9.8	0.49	0.68	0.29	2.68
7	9.2	0.49	0.68	0.29	2.65

Table 2. Values of $\phi_{D_2O}(\infty)$, τ_1, B_1, R, and D_c of the Interface Part of the P(S-*b*-NIPAM) Film

cycle no.	$\phi_{D_2O}(\infty)$	$\tau_1/10^4$ s	B_1	R	$D_c/10^{-18}$ cm^2/s
1	38	0.5	0.68	0.29	7.23
2	37.5	0.5	0.66	0.29	6.98
3	36.5	0.5	0.68	0.29	7.07
4	34	0.47	0.68	0.29	7.25
5	33.5	0.47	0.72	0.34	7.98
6	32.8	0.44	0.68	0.29	7.61
7	32	0.43	0.72	0.34	8.53

In the final cycles this decrease stops, which demonstrates that the aging is not continuing. Only the values of D_c, which is related to the final thickness of the film Z_∞, is much smaller (factor 6−9) than those of the literature[6,67] because our film thickness is in the nanometer scale.

Figure 7b shows the water uptake of the interface part of the film (bottom layer) versus time. Table 2 summarizes the values of $\phi_{D_2O}(\infty)$, τ_1, B_1, R, and D_c resulting from a fit with the model described above.

As Table 2 shows, the values of τ_1 and D_c have only a slight decrease, and the values of B_1 and R are nearly constant. The values of B_1 and R of the interface layer are nearly the same as those of the main layer during the last cycles. For comparison, the resulting relaxation times of both parts are shown in Figure 7c.

Regarding relaxation times, it is worth noting that pure, thick PNIPAM homopolymer gel films follow the same behavior but with a strong thickness increase.[53] The relaxation times of pure PNIPAM gel film were 530 s at 21 °C and 810 s at 25 °C. For the investigated P(S-*b*-NIPAM) film the relaxation times of the main part of the film are larger than the ones of the interface part. For the main part of the initially prepared film, $\tau_1 = 660$ s is determined at 23 °C, which compares well with the observations by Zhou and Wu.[53] Thus, diffusion in the second regime is driven by the PNIPAM domains. However, in contrast to PNIPAM gel films, in the investigated P(S-*b*-NIPAM) film the volume fraction of the PS domain takes a dominant role (72.4%), and thus the total swelling is seriously restricted.

In summary, the mechanism of the water storage and water removal in cyclic switching of the P(S-*b*-NIPAM) film is described in Scheme 2. In a first stage (stage 1), the water molecules diffuse into all accessible volume of the whole P(S-*b*-NIPAM) film. Next, in a second stage (stage 2), the PNIPAM chains are in contact with the water molecules and swell but are restricted by the PS domains, which causes a slight reorganization of the initial microphase separation morphology (overemphasized for clarity in Scheme 2). Third (stage 3), after extraction of the water by applying vacuum, the PNIPAM cannot relax back totally because of the restriction by the PS domains and deformations remain. The resulting structure serves as the input for the next swelling, again starting with the stage 1 process, but water molecules enter in a modified P(S-*b*-NIPAM) film. After several repeated cycles, the PNIPAM structures equilibrate

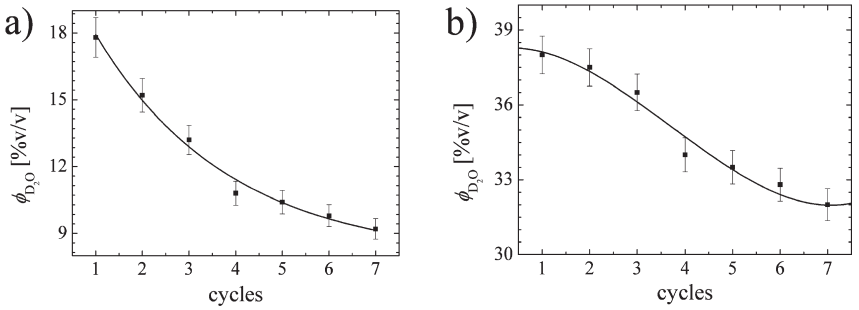

Figure 8. Maximum water absorption of the P(S-*b*-NIPAM) film at the end of each water storage cycle plotted as a function of the cycle number: (a) for the main part of the film and (b) for the interface part of the film.

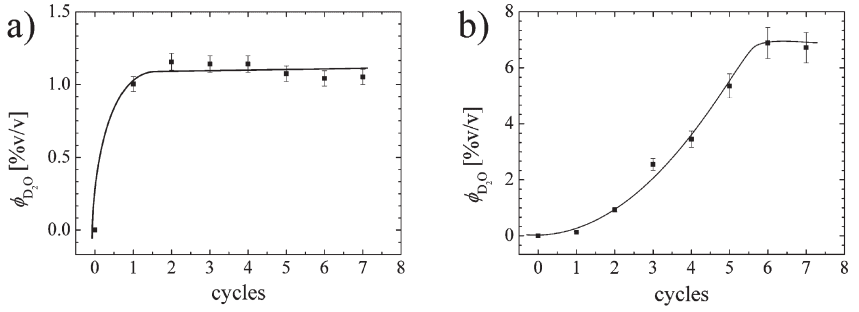

Figure 9. The remaining water in the P(S-*b*-NIPAM) film at the end of each removal of the water vapor plotted as a function of the storage and removal cycle: (a) for the main part of the film and (b) for the interface part of the film.

in a different and, with respect to the water storage capacity, less favorable morphology.

d. Aging during Cyclic Switching. The aging of the P(S-*b*-NIPAM) film in terms of the water storage capacity is visualized by the maximum water absorption of the P(S-*b*-NIPAM) film at the end of each water storage cycle shown in Figure 8. In fact, in the first four cycles for the entire film the aging is stronger than in the subsequent three cycles. During the first four cycles, for the main part of the film the maximum storage capacity decreases from 17.8 to 10.8%. However, from the fourth cycle to the seventh cycle, it only decreases slightly (from 10.8% to 9.2%), which shows that the film gradually reaches the equilibrium state of aging. With respect to application such a behavior is advantageous. The film can be reused for water storage and aging slows down.

In contrast to the behavior of the main part of the film, the interface part (pure PNIPAM) has a stronger ability of water storage. It absorbs 38% water at the end of the first water storage cycle. Moreover, as compared to the main part it does not show an as high reduction in the water storage ability with increasing cycle number. In the interface part of the film, consisting of pure PNIPAM, the decrease of the stored water volume fraction decreases from initially 38 to 32% after seven cycles. The difference between the main part and the interface part of the film in terms of aging hints that the main reason for such decrease is due to a structural reorganization of the microphase-separated structure, whereas the pure PNIPAM part undergoes more reversible changes.

The initial structure of the P(S-*b*-NIPAM) film results from its preparation out of 1,4-dioxane solution. Because dioxane is much less selective for both blocks of the diblock copolymer than water, the structure is different from the one which would have been observed from aqueous solution. After being in contact with water, caused by the absorption of water from the water vapor, the glassy and water-insoluble PS blocks confine the swelling of the water-soluble PNIPAM blocks. The morphology starts to slightly rearrange within the spatial confinement introduced by the glassy PS matrix which introduces the deformation and slight destruction of the initially formed PNIPAM structures (see Scheme 2). GISAXS and AFM reveal that this change is due to a domain formation whereas the local microphase separation structure (cylinders of PNIPAM in a matrix of PS) is unaffected. After several cycles, the water incorporation ability of PNIPAM blocks is reduced but finally reaches an equilibrium state, which is again important for applications which require cyclic water storage.

e. H−D Exchange Reaction. From the neutron reflectivity data measured before each storage cycle and after water removal, slight modifications of the P(S-*b*-NIPAM) film were observed (see Figure 4). These changes cannot be explained by the rearrangement of the P(S-*b*-NIPAM) film. Any rearrangement of the PS and PNIPAM domains, both being fully protonated, cannot explain an increase in SLD. Deuterated material (D_2O) needs to be involved to explain such increase of the SLD. From the measured increase in SLD the amount of remaining water in the P(S-*b*-NIPAM) film is determined (see Figure 9). The main and interface part of the film behave differently. After one cycle, in the main part of the film ~1% v/v water remains. Within the error bar this values stays unchanged for the subsequent six cycles. In contrast, in the interface part of the film, the amount of remaining water increases during the first six cycles and reaches an equilibrium value of 7% v/v significantly later. Such a difference can be caused either by the composition of the different parts (main vs interface−P(S-*b*-NIPAM) vs PNIPAM) or by the interaction with Si substrate.

The remaining water can be caused by formation of strong chemical bonds between D_2O and PNIPAM molecules (bound water). Alternatively, H−D exchange occurring during water storage inside the film can give the impression of not extractable water. To get independent information, we

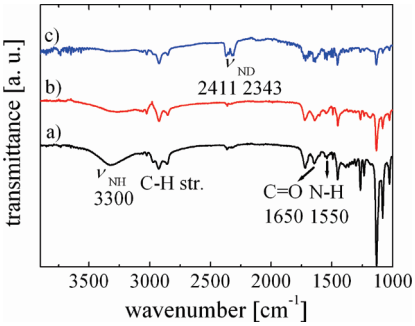

Figure 10. IR spectra of P(S-*b*-NIPAM) film: (a) as prepared, (b) after exposure to H_2O at 296 K for 30 min followed by drying in air at 296 K for 15 min, and (c) after exposure to D_2O at 296 K for 30 min followed by drying in air at 296 K for 15 min.

used FTIR on the P(S-*b*-NIPAM) film before and after exposure to the vapor of H_2O and D_2O for 30 min at 23 °C. The results are shown in Figure 10. For the dry P(S-*b*-NIPAM) film, two bands due to NH_2 groups were observed at 3300 and 1541 cm^{-1}, which result from N−H stretching. Besides these bands, the absorption bands in the range of 2800−3000 and 1650 cm^{-1}, assigned to C−H stretching and the characteristic peak of the C=O, are observed, respectively. After the dry film exposure to H_2O vapor for 30 min and drying in air for 15 min, there was no change except that the 3300 cm^{-1} band is dampened and broadened.

However, when the dry P(S-*b*-NIPAM) film was exposed to the D_2O vapor for 30 min and then dried in air for 15 min, the bands due to NH_2 disappeared, and two bands appeared at 2411 and 2343 cm^{-1}. These bands are attributed to asymmetric and symmetric N−D stretching. We conclude that the exchange reaction between NH_2 and D_2O occurred during the water storage. The exchange probably proceeds via anionic intermediates. This indicates that the basic strength of the $-NH_2$ group of P(S-*b*-NIPAM) is stronger than the pK_a value of D_2O. Consequently, H−D exchange has to be considered and is the origin of the apparently remaining water. Thus, the FTIR result is in good agreement with the GISAXS observation, and we can exclude residual solvent being deposited during cycling.

4. Summary

Using P(S-*b*-NIPAM) with a long PS and a short PNIPAM block in combination with a solvent, which is more equal in interaction with the both blocks than water, results in thin films, which allow for water storage without swelling. The installed glassy matrix suppresses the swelling inherent for hydrogel films (e.g., PNIPAM films) and gives the necessary stability to enable repeated water storage. Although the internal rearrangement of the structure installed out of 1,4-dioxane during storage cycles decreases the amazingly high capability of incorporating close to 17% water in total without swelling, aging of the films is limited. Aging stops after several storage cycles, and a reduced water storage capacity remains.

The mechanisms of the water storage and water removal do not depend on the cycle number (see Scheme 2). With the investigated glassy films, we have a new material at hand which allows repeated storage of water at fixed volume or fixed film thickness conditions. Thus, this material will avoid problems related to swelling induced strain. It can be used for coatings reducing humidity in nanoapplications, which might suffer from changes in the water content of the surrounding atmosphere.

Acknowledgment. We thank S. V. Roth for the help with setting up the BW4 instrument at HASYLAB and S. Prams, M. A. Ruderer, and Q. Zhong for their help during the GISAXS measurements. Financial support by Deutsche Forschungsgemeinschaft (DFG) in the priority program SPP 1259 (MU1487/8 and PA771/4) is gratefully acknowledged.

References and Notes

(1) Hui, C. Y.; Wu, K. C.; Lasky, R. C.; Kramer, E. J. *J. Appl. Phys.* **1987**, *61*, 5129.
(2) Hui, C. Y.; Wu, K. C.; Lasky, R. C.; Kramer, E. J. *J. Appl. Phys.* **1987**, *61*, 5137.
(3) Gall, T. P.; Kramer, E. J. *Polymer* **1991**, *32*, 265.
(4) Durning, C. J.; Hassan, M. M.; Tong, H. M.; Lee, K. W. *Macromolecules* **1995**, *28*, 4234.
(5) Stamatialis, D. F.; Sanopoulou, M.; Raptis, I. *J. Appl. Polym. Sci.* **2002**, *83*, 2823.
(6) Thompson, R. L.; McDonald, M. T.; Lenthall, J. T.; Hutchings, L. R. *Macromolecules* **2005**, *38*, 4339.
(7) Müller-Buschbaum, P.; Bauer, E.; Maurer, E.; Cubitt, R. *Physica B* **2006**, *385−386*, 703.
(8) Müller-Buschbaum, P.; Bauer, E.; Maurer, E.; Nelson, A.; Cubitt, R. *Phys. Status Solidi RRL* **2007**, *1*, R68.
(9) Perlich, J.; Körstgens, V.; Metwalli, E.; Schulz, L.; Georgii, R.; Müller-Buschbaum, P. *Macromolecules* **2009**, *42*, 337.
(10) Smith, C. P.; Fritz, D. C.; Tirrell, M.; White, H. S. *Thin Solid Films* **1991**, *198*, 369.
(11) Wang, W.; Metwalli, E.; Perlich, J.; Troll, K.; Papadakis, C. M.; Cubitt, R.; Müller-Buschbaum, P. *Macromol. Rapid Commun.* **2009**, *30*, 114.
(12) Winnik, F. M. *Macromolecules* **1990**, *23*, 233.
(13) Schild, H. G. *Prog. Polym. Sci.* **1992**, *17*, 163.
(14) Tam, K. C.; Wu, X. Y.; Pelton, R. H. *J. Polym. Sci., Polym. Chem. Ed.* **1993**, *31*, 963.
(15) Tiktopulo, E. I.; Bychkova, V. E.; Ricka, J.; Ptitsyn, O. B. *Macromolecules* **1994**, *27*, 2879.
(16) Wu, C.; Zhou, S. *Macromolecules* **1995**, *28*, 8381.
(17) Wang, X.; Qiu, X.; Wu, C. *Macromolecules* **1998**, *31*, 2972.
(18) Pelton, R. *Adv. Colloid Interface Sci.* **2000**, *85*, 1.
(19) Maeda, Y.; Higuchi, T.; Ikeda, I. *Langmuir* **2001**, *17*, 7535.
(20) Stieger, M.; Richtering, W. *Macromolecules* **2003**, *36*, 8811.
(21) Kita, R.; Wiegand, S. *Macromolecules* **2005**, *38*, 4554.
(22) Lutz, J.-F.; Akfemir, Ö.; Hoth, A. *J. Am. Chem. Soc.* **2006**, *128*, 13046.
(23) Stieger, M.; Richtering, W. *Macromolecules* **2003**, *36*, 8811.
(24) Kujawa, P.; Segui, F.; Shaban, S.; Diab, C.; Okada, Y.; Tanaka, F.; Winnik, F. M. *Macromolecules* **2006**, *39*, 341.
(25) Ye, J.; Xu, J.; Hu, H.; Wang, X.; Zhang, G.; Liu, S.; Wu, C. *Macromolecules* **2008**, *41*, 4416.
(26) Zhou, K.; Lu, Y.; Li, J.; Shen, L.; Zhang, G.; Xie, Z.; Wu, C. *Macromolecules* **2008**, *41*, 8927.
(27) Koga, T.; Tanaka, F.; Motokawa, R.; Koizumi, S.; Winnik, F. M. *Macromolecules* **2008**, *41*, 9413.
(28) Durand, A.; Hourdet, D. *Polymer* **1999**, *40*, 4941–4951.
(29) Durand, A.; Hourdet, D.; Lafuma, F. *J. Phys. Chem. B* **2000**, *104*, 9371–9377.
(30) Lin, H.-H.; Cheng, Y.-L. *Macromolecules* **2001**, *34*, 3710–3715.
(31) Hietala, S.; Nuopponen, M.; Kalliomäki, K.; Tenhu, H. *Macromolecules* **2008**, *41*, 2627.
(32) Nykänen, A.; Nuopponen, M.; Hiekkataipale, P.; Hirvonen, S.-P.; Soininen, A.; Tenhu, H.; Ikkala, O.; Mezzenga, R.; Ruokolainen, J. *Macromolecules* **2008**, *41*, 3243.
(33) Huber, D. L.; Manginell, R. P.; Samara, M. A.; Kim, B. I.; Bunker, B. C. *Science* **2003**, *301*, 352.
(34) Nuopponen, M.; Ojala, J.; Tenhu, H. *Polymer* **2004**, *45*, 3643.
(35) Hellweg, T.; Dewhurst, C. D.; Eimer, W.; Kratz, K. *Langmuir* **2004**, *20*, 4330.
(36) Zhang, W.; Zhou, X.; Li, H.; Fang, Y.; Zhang, G. *Macromolecules* **2005**, *38*, 909.
(37) Troll, K.; Kulkarni, A.; Wang, W.; Darko, C.; Bivigou Koumba, A. M.; Laschewsky, A.; Müller-Buschbaum, P.; Papadakis, C. M. *Colloid Polym. Sci.* **2008**, *286*, 1079.
(38) Nykänen, A.; Nuopponen, M.; Laukkanen, A.; Hirvonen, S.-P.; Rytela, M.; Turunen, O.; Tenhu, H.; Mezzenga, R.; Ikkala, O.; Ruokolainen, J. *Macromolecules* **2007**, *40*, 5827–5834.
(39) Zhou, X.; Ye, X.; Zhang, G. *J. Phys. Chem. B* **2007**, *111*, 5111.
(40) Jain, A.; Kulkarni, A.; Bivigou Koumba, A. M.; Wang, W.; Busch, P.; Laschewsky, A.; Müller-Buschbaum, P.; Papadakis, C. M. *Macromol. Symp.*, in press.

(41) Wang, W.; Troll, K.; Kaune, G.; Metwalli, E.; Ruderer, M.; Skrabania, K.; Laschewsky, A.; Roth, S. V.; Papadakis, C. M.; Müller-Buschbaum, P. *Macromolecules* **2008**, *41*, 3209.
(42) Steitz, R.; Leiner, V.; Tauer, K.; Khrenov, V.; v. Klitzing, R. *Appl. Phys. A: Mater. Sci. Process.* **2002**, *74*, S519.
(43) Yim, H.; Kent, M. S.; Huber, D. L.; Satija, S.; Majewski, J.; Smith, G. S. *Macromolecules* **2003**, *36*, 5244.
(44) Yim, H.; Kent, M. S.; Mendez, S.; Lopez, G. P.; Satija, S.; Seo, Y. *Macromolecules* **2006**, *39*, 3420.
(45) Alves de Rezende, C.; Lee, L.-T.; Galembeck, F. *Langmuir* **2008**, *24*, 7346.
(46) Schmidt, S.; Motschmann, H.; Hellweg, T.; von Klitzing, R. *Polymer* **2008**, *49*, 749.
(47) Müller-Buschbaum, P. *Eur. Phys. J. E* **2003**, *12*, 443.
(48) Cubitt, R.; Fragneto, G. *Appl. Phys. A: Mater. Sci. Process.* **2003**, *74*, 329.
(49) Nelson, A. *J. Appl. Crystallogr.* **2006**, *39*, 273.
(50) Parrat, L. G. *Phys. Rev. B* **1954**, *95*, 359.
(51) Roth, S. V.; Döhrmann, R.; Dommach, M.; Kuhlmann, M.; Kröger, I.; Gehrke, R.; Walter, H.; Schroer, C.; Lengeler, B.; Müller-Buschbaum, P. *Rev. Sci. Instrum.* **2006**, *77*, 085106.
(52) Müller-Buschbaum, P. *Anal. Bioanal. Chem.* **2003**, *376*, 3.
(53) Zhou, S.; Wu, C. *Macromolecules* **1996**, *29*, 4998–5001.
(54) Lawrence, C. J. *Phys. Fluids* **1988**, *31*, 2786.
(55) Spangler, L. L.; Torkelson, M.; Royal, J. S. *Polym. Eng. Sci.* **1990**, *30*, 644.
(56) Schubert, D. W. *Polym. Bull.* **1997**, *38*, 177.
(57) Müller-Buschbaum, P.; Bauer, E.; Wunnicke, O.; Stamm, M. *J. Phys.: Condens. Matter* **2005**, *17*, S363.
(58) Richter, A.; Howitz, S.; Kuckling, D.; Arndt, K. F. *Sens. Actuators, B* **2004**, *99*, 451.
(59) Schmidt, T.; Mönch, J. I.; Arndt, K. F. *Macromol. Mater. Eng.* **2006**, *291*, 755.
(60) Bhatnagar, P.; Strickland, A. D.; Kim, I.; Malliaras, G. G.; Batt, C. A. *Appl. Phys. Lett.* **2007**, *90*, 144107.
(61) Gonuguntla, M.; Sharma, A.; Subramanian, S. A. *Macromolecules* **2006**, *39*, 3365.
(62) Dingenouts, N.; Seelenmeyer, S.; Deike, I.; Rosenfeldt, S.; Ballauff, M.; Lindner, P.; Narayanan, T. *Phys. Chem. Chem. Phys.* **2001**, *3*, 1169.
(63) Müller-Buschbaum, P.; Maurer, E.; Bauer, E.; Cubitt, R. *Langmuir* **2006**, *22*, 9295.
(64) Tanaka, T.; Fillmore, D. *J. Chem. Phys.* **1990**, *92*, 1365.
(65) Peters, A.; Candau, S. J. *Macromolecules* **1988**, *21*, 2278.
(66) Li, Y.; Tanaka, T. *J. Chem. Phys.* **1990**, *92*, 1365.
(67) Zhou, S.; Wu, C. *Macromolecules* **1996**, *29*, 4998.
(68) Wu, C.; Yan, C.-Y. *Macromolecules* **1994**, *27*, 4516.
(69) Zrinyi, M.; Rosta, J.; Horkay, F. *Macromolecules* **1993**, *26*, 3097.